PHYSICAL REVIEW ACCELERATORS AND BEAMS **27,** 084501 (2024)

Simulation and measurement of beam-induced heating of ceramic vacuum chambers

Aamna Khan,[*] Gabriele Bassi, Bernard Kosciuk, Robert Todd, Victor Smaluk,
Belkacem Bacha, Paul Palecek, and Charles Hetzel
Brookhaven National Laboratory, Upton, New York 11973-5000, USA

(Received 18 December 2023; accepted 29 July 2024; published 9 August 2024)

In this article, we summarize recent theoretical and experimental studies of the impedance and beam-induced heating of titanium-coated ceramic vacuum chambers used in the NSLS-II injection kickers. The impedance was calculated using the field matching theory assuming planar approximation and compared with the ImpedanceWake2D code. For the coating thickness of a few microns, we demonstrated that the beam-induced power is dissipated in the titanium coating and that the longitudinally averaged two-dimensional power density is approximated by an analytical expression, thus allowing the use of a simplified model of the power density as input for the ANSYS code to simulate the temperature distribution with realistic nonuniform thickness of the Ti coating. For a few values of the NSLS-II beam current, we measured the beam-induced heating of two ceramic chambers using thermal sensors installed along the chamber and compared the measurement results with the simulations.

DOI: 10.1103/PhysRevAccelBeams.27.084501

I. INTRODUCTION

Vacuum chambers made of high-performance ceramics are fundamental components of pulsed magnets used in particle accelerators for injection and extraction of beams. Ceramic chambers are extremely resistant to heat, corrosion, and chemical influences [1]. However, such a chamber functions as a slow-wave structure with large coupling impedance, a phenomenon intrinsically linked to the ceramic material's significant resistivity and permittivity [2]. These properties are fundamental to the chamber's behavior, contributing to the accumulation of static charges on the ceramic surface. For reliable discharge of image current and reduction of the impedance, the inner surfaces of the ceramic chambers are coated with a metal, usually titanium (Ti). The flaws of such a coating are obvious: it affects the kicker efficiency by partially shielding the beam from the external magnetic field and heats the chamber walls due to eddy currents [3]. It is important to find a reasonable thickness of Ti coating [4,5], which is a trade-off of two contradictory requirements: (i) the coating must be thick enough to minimize the impedance for eddy currents and (ii) thin enough to minimize shielding effect resulting in deterioration of the pulse magnetic field kicking the beam.

In this paper, we present a comprehensive theoretical and experimental study of the beam-induced heating of Ti-coated ceramic vacuum chambers, recently completed at NSLS-II. The schematic of the ceramic chambers installed in NSLS-II injection kickers is shown in Fig. 1. The chambers have an octagonal profile measuring $76\ \mathrm{mm}\ (\mathrm{H}) \times 24.3\ \mathrm{mm}\ (\mathrm{V})$, the length of ceramics is 815 mm, and the thickness is 6.4 mm. This profile matches the cross section of the adjacent bellows and chambers. The original specification for the kicker ceramic chambers called for a 2 to 5-μm-thick coating of Ti on the entire inner surface.

In this work, we do not consider the ferrite layer. At higher frequencies, the skin depth is very small, leading to minimal penetration of electromagnetic fields beyond the surface layer. In Sec. III, we have also demonstrated that, with a coating thickness of just a few microns, the beam-induced power is efficiently dissipated within the titanium coating itself. This, combined with the screening effect provided by the ceramic layer and air gap, ensures that the electromagnetic fields from the beam have negligible interaction with the ferrite layer.

Our study aims to address the challenges associated with the overheating of these chambers, which have been observed to impact the reliable operation of particle accelerators. By combining simulations with experimental measurements, we aim to gain a deeper understanding of the impedance characteristics and heat distribution within the ceramic chambers.

The paper is organized as follows: In Sec. II, we provide a brief overview of heating issues encountered at different accelerator facilities, such as BESSY II, ESRF-EBS, HLS,

---

[*] Contact author: akhan1@bnl.gov

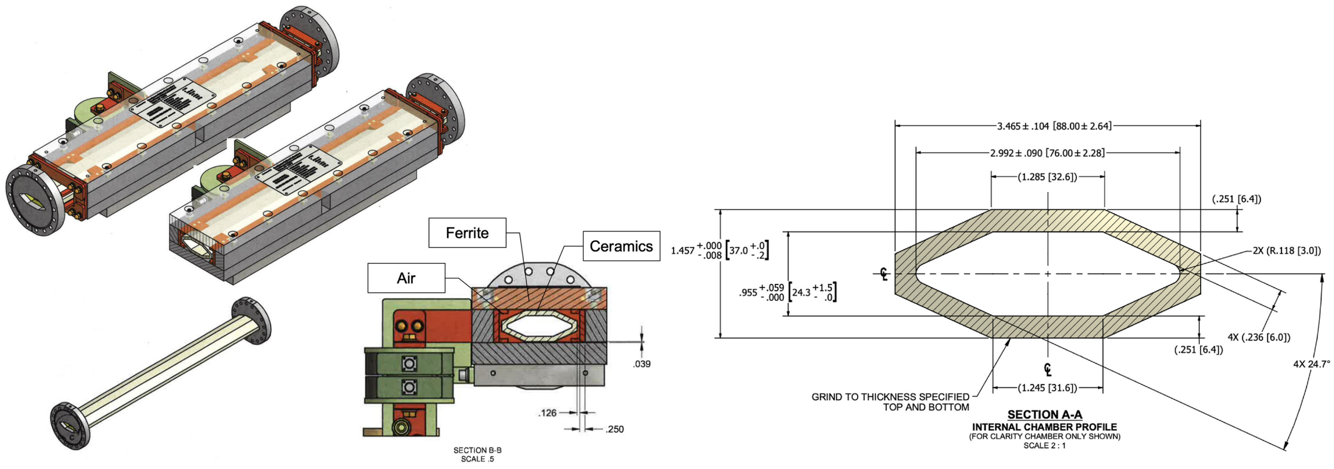

FIG. 1. Schematic of the NSLS-II kicker chamber.

MAX-IV, SOLEIL, and NSLS-II. By extracting insights from these experiences, we gain valuable knowledge about the impact of the ceramic-coating thickness and the uniformity on chamber performance. In Sec. III, we present the theoretical framework, which, in addition to calculating the beam power loss, allows for the computation of Ohmic losses on the electromagnetic layers. To validate our theoretical model, we benchmark a closed formula for the longitudinal impedance against the ImpedanceWake2D (IW2D) [6] computing code. To experimentally test our theoretical predictions, we carried out testbench measurements of resistivity and beam-based measurements of beam-induced heating for two chambers, SN003 and SN001, as explained in Sec. IV. Finally, in Sec. V, we describe the thermal analysis and compare the simulations with experimental data.

II. CERAMICS HEATING ISSUES IN ACCELERATORS

Several accelerator facilities including BESSY-II [7], ESRF-EBS [8], HLS [9], SOLEIL [10,11], MAX-IV [12], and NSLS-II [13] reported overheating of their Ti-coated ceramics chambers due to lack of coating uniformity with appropriate thickness or/and poor coating adhesion. Therefore, to avoid failure of ceramic chambers due to thermal stress cracking, a sequence of simulations is usually performed to calculate the EM fields, impedance, heat source distribution, and temperature map for a given ceramic shape and loss tangent.

A prototype in Ref. [7] at BESSY-II showed that even though the injection outmatched expectations, the strong interaction with the stored beam resulted in high heat load causing the 5-μm-thin Ti-coated ceramic chamber to reach temperatures over 500 °C and fail. The operations at MAX-IV made known that heating issues of ceramic chambers arise for a thin coating of 1 μm and further studies [12,14] stated that a thicker coating would be preferable.

Because of its complex shape, the ESRF-EBS vacuum chamber is constructed of four pieces of ceramics that have been glazed together [15]. However, the chamber cracked at the glazing location due to overheating during the first time ramp up of the beam current [8].

During the commissioning of the new MIK pulsed magnet at SOLEIL, excessive heating in the MIK chamber and flanges was resolved by adding cooling fans. This underscores the need for accurate thermal load estimation and suggests potential design improvements, such as thermal simulations and adjusting coating thickness, albeit with potential of field perturbation trade-offs [11].

At NSLS-II, concerns over the excessive heating measured in the kicker chambers prompted an inspection of their interior. Once opened, it was discovered that the Ti coating was damaged, and there was a significant color change of the ceramics compared to a spare chamber. This issue was critical to address for achieving the 500 mA design current at NSLS-II. Cooling fans were installed for temporary mitigation of the overheating and then, as a reliable long-term solution, a tool for in-house coating of ceramic chambers has been designed, built, and commissioned [13,16,17].

III. FIELD MATCHING THEORY

We applied the field matching theory (FMT) to the model shown in Fig. 2. Following the analytical approach adopted in [18], in [19] the model has been extended to consider two parallel layers with arbitrary complex relative permittivity and permeability. A deeper analysis with complete derivations is discussed in a companion paper [20].

A. Longitudinal impedance formula

A general formula [21] for the longitudinal impedance per unit length $Z_0^{||}/L$, where L is the length of the impedance structure, is given in [19]. Here we give a simplified version of the formula assuming the condition $k/\xi \ll 1$, which is very well satisfied for frequencies below 100 GHz corresponding to the frequency range of our interest:

$$\frac{Z_0^{||}}{L} = i\frac{Z_0}{4\pi}k\int_{-\infty}^{+\infty}\frac{q(a_1+a_2d_1)\,\mathrm{sech}^2 bq}{qq_1(a_3+a_4d_1)+(q^2-k^2)(a_5+a_6d_1)\tanh\,bq}dq, \tag{1}$$

where $Z_0 \approx 377\ \Omega$ and

$$\begin{gathered} a_1 = b_1 - b_2 - b_3 + b_4 + b_5, \qquad a_2 = b_1 + b_2 + b_3 + b_4 + b_5, \qquad a_3 = -b_1 - b_2 + b_3 - b_4 - b_5, \\ a_4 = b_1 - b_2 + b_3 + b_4 + b_5, \qquad a_5 = b_1 - b_2 - b_3 + b_4 + b_5, \qquad a_6 = b_1 + b_2 + b_3 - b_4 + b_5, \\ b_1 = (\varepsilon_2 - 1)(q^2 - k^2)q_1q_2(d_2^2 - 1), \qquad b_2 = q(q_2^2 - q^2)(2(d_2 - 1)^2 q + (d_2^2 - 1))q_2(1 + \varepsilon_2), \\ b_3 = (q^2 - k^2)((d_2 + 1)^2 q_2^2 \varepsilon_2 - (d_2 - 1)^2 q_2^2), \qquad b_4 = qq_1q_2^2((d_2 - 1)^2 + (d_2 + 1)^2\varepsilon_2), \qquad b_5 = 2q^2q_1q_2(d_2^2 - 1), \\ d_1 = e^{2q_1\tau_1}, \qquad d_2 = e^{2q_2\tau_2}, \qquad q_1 = \sqrt{q^2 - ik\xi}, \qquad \xi = Z_0\sigma_c, \qquad q_2 = \sqrt{q^2 - k^2(\varepsilon_2 - 1)}, \qquad \varepsilon_2 = \varepsilon'(1 + i\tan\delta), \end{gathered} \tag{2}$$

where σ_c is the electrical conductivity of the Ti-coating layer, ε_2 the complex permittivity of the ceramic chamber, with $\tan\delta$ the tangent loss factor, τ_1 and τ_2 the thickness of the Ti-coating layer and ceramic chamber, respectively, and b is the ceramic chamber half-aperture.

A further good approximation, not essential for our derivation of Eq. (1), consists of neglecting the term q^2 in the expression of q_1 given by Eq. (2), leading for q_1 to the result $q_1 = \sqrt{k\xi/2}(i-1)$. We note that the coefficients given by Eq. (2) do not depend on b.

B. Benchmark theory with IW2D simulations

The impedance of the ceramic chamber is estimated using IW2D, a code developed at CERN to compute longitudinal and transverse impedance in a two-dimensional multilayered flat structure. The number of layers can be arbitrary depending on the user application requirement, and each of them can be made of any linear homogeneous isotropic stationary material. The last layer, which can also be vacuum, should always be modeled with infinite thickness and with low conductivity. The code relies on the analytic computation of the electromagnetic fields created by a point-charge beam traveling at any speed in the whole structure. The details of flat structure impedance formalism are discussed in [22,23].

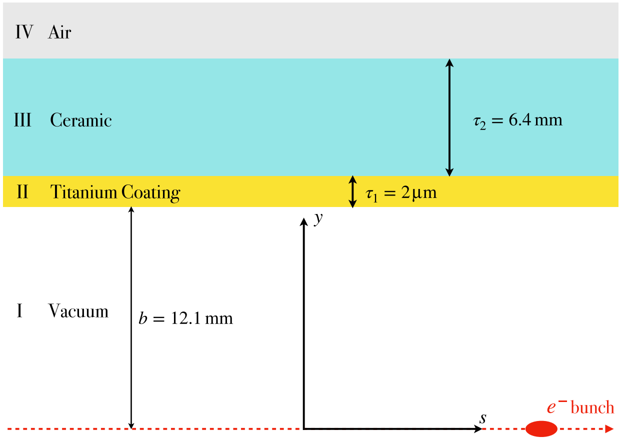

FIG. 2. Geometry of the vacuum chamber in planar approximation.

We simulate the NSLS-II kicker chamber with the half-height of $b = 12.1$ mm as a three-layer flat structure composed of a 6.4-mm-thick ceramic chamber with two thickness values of Ti coating $\tau_1 = 0.55, 1.21$ μm, plus the last infinite layer. The material properties for the IW2D calculations are given in Table I.

Figure 3 shows the comparison of the longitudinal impedance obtained from IW2D and from the field matching theory discussed above, i.e., from the numerical integration of Eq. (1), for the NSLS-II chambers with different Ti-coating thickness. There is a good agreement between the theoretical and IW2D calculations.

C. Beam-induced power and Ohmic losses

In the following discussion, we use the scalar symbol I to label the average current while the vector symbol $\boldsymbol{J}$ to label current densities. In order to avoid the repeated use of current density, we simply use current for $\boldsymbol{J}$. According to Ampere's law, the total effective current reads

$$\boldsymbol{J}(\boldsymbol{r},t) = \boldsymbol{J}_f(\boldsymbol{r},t) + \frac{\partial}{\partial t}\boldsymbol{D}(\boldsymbol{r},t) =: \boldsymbol{J}_f(\boldsymbol{r},t) + \boldsymbol{J}_D(\boldsymbol{r},t), \tag{3}$$

where $\boldsymbol{J}_f$ represents the *external* or *free* current, and the displacement current $\boldsymbol{J}_D = \boldsymbol{J}_c + \boldsymbol{J}_d$, where $\boldsymbol{J}_c$ represents

TABLE I. Material properties of Ti-coated ceramic chambers for comparison between IW2D and FMT.

Layers	ρ (Ωm)	$\tan(\delta)$	ϵ'	τ (μm)
Ti	4.3×10^{-7}	0	1	0.55, 1.21
Ceramics	5×10^5	1×10^{-3}	10	6.4×10^3
Vacuum	Infinity	0	1	Infinity

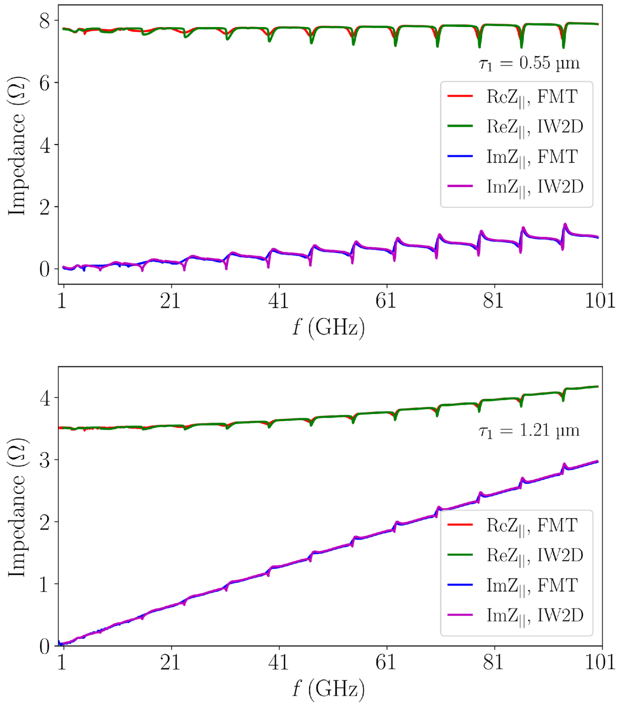

FIG. 3. Comparison of the Ti-coated ceramic chamber impedance for coating thickness of $\tau_1 = 0.55$ and 1.21 μm with IW2D and FMT.

the *conduction* current (due to unbound conduction charges) and $\boldsymbol{J}_d$ represents the *dielectric* or *polarization* current (due to bound polarized charges).

Applying conservation of energy, Poynting's theorem states that in the volume occupied by our electromagnetic structure, the stored energy u changes at a rate given by the work done on the charges within the volume, minus the rate r at which energy leaves the volume [24]. If we assume $u = \text{const}$ and $r = 0$, Poynting's theorem implies that the power lost by the beam (free current $\boldsymbol{J}_f$) equals the power dissipated due to Ohmic losses (displacement current $\boldsymbol{J}_D$) [25]

$$P_{\text{loss}} = P_{\text{ohm}}, \tag{4}$$

where

$$P_{\text{loss}} = \int d^3\boldsymbol{r}\boldsymbol{J}_f(\boldsymbol{r},t)\cdot\boldsymbol{E}(\boldsymbol{r},t),$$
$$P_{\text{ohm}} = \int d^3\boldsymbol{r}\boldsymbol{J}_D(\boldsymbol{r},t)\cdot\boldsymbol{E}(\boldsymbol{r},t), \qquad \boldsymbol{r} = (z,x,y). \tag{5}$$

The total power lost by M Gaussian bunches with length σ_τ and average current I_0 traversing an impedance structure of length L reads

$$P_{\text{loss,T}} = -T_0\frac{I_0^2}{M}k_{\text{loss}},$$
$$k_{\text{loss}} = \frac{1}{\pi}\int_0^\infty d\omega e^{-\omega^2\sigma_\tau^2}\,\text{Re}Z_0^{||}(\omega), \tag{6}$$

where T_0 is the revolution period. The integral summation in Eq. (6) is justified by the fact that the impedance is broadband [26].

For the rest of this paper, we use s instead of z to label the longitudinal coordinate. In order to take into account the variation of the Ti-coating thickness with longitudinal position s, as shown in Fig. 6, we assume the Ti-coating thickness τ_1 piece-wise constant over the length Δ, with $\Delta = 28.1$ mm. It follows that the total beam-induced power loss reads

$$P_{\text{loss,T}} = -T_0\frac{I_0^2}{M}\sum_{n=1}^{N}k_{\text{loss,n}},$$
$$k_{\text{loss,n}} = \frac{1}{\pi}\int_0^\infty d\omega e^{-\omega^2\sigma_\tau^2}\text{Re}Z_0^{||}[\omega;\tau_1(s_n)],$$
$$s_n = n\Delta, \quad N = 29, \tag{7}$$

where the explicit dependence of the Ti-coating thickness τ_1 on the longitudinal position s_n has been inserted in the argument of $\text{Re}Z_0^{||}$, and in the use of Eq. (1), we set $L = \Delta$.

Assuming $\boldsymbol{J}_D = \boldsymbol{J}_c$ in the metal coating and $\boldsymbol{J}_D = \boldsymbol{J}_d$ in the ceramic chamber, Ohmic losses are determined by the power dissipated in the metal coating (conduction losses) plus the power dissipated in the ceramic chamber (dielectric losses)

$$P_{\text{ohm}} = P_{\text{cond}} + P_{\text{diel}}, \tag{8}$$

where, with the use of Ohm's law $\boldsymbol{J}_c = \sigma_c\boldsymbol{E}$,

$$P_{\text{cond}} = \sigma_c\int d^3\boldsymbol{r}\boldsymbol{E}(\boldsymbol{r},t)\cdot\boldsymbol{E}(\boldsymbol{r},t),$$
$$P_{\text{diel}} = \int d^3\boldsymbol{r}\boldsymbol{J}_d(\boldsymbol{r},t)\cdot\boldsymbol{E}(\boldsymbol{r},t). \tag{9}$$

For a general thermal analysis, the power density $\boldsymbol{J}_D\cdot\boldsymbol{E}$ is calculated inside every electromagnetic layer. In [20], the calculation is discussed using the general expression of the displacement current $\boldsymbol{J}_D$ adopting the Lorentz oscillator model. In this paper, we use the following results [27]: (i) with the range of variation of the Ti-coating thickness as given in Fig. 6, with good approximation all the power is dissipated on the metal coating, i.e., $P_{\text{ohm}} \simeq P_{\text{cond}}$, $P_{\text{diel}} \simeq 0$; (ii) the averaged three-dimensional power density $P_3(s,x,y)$ on the metal coating can be cast in the following form using Eq. (7):

$$P_3(s_n,x,y) = \frac{P_{\text{loss},n}}{2\Delta\tau_1(s_n)}G(x), \qquad G(x) = \frac{A}{\cosh^2(\frac{\pi}{2b}x)},$$
$$A = \left(\int\frac{dx}{\cosh^2(\frac{\pi}{2b}x)}\right)^{-1} = \frac{\pi}{4b}, \tag{10}$$

where

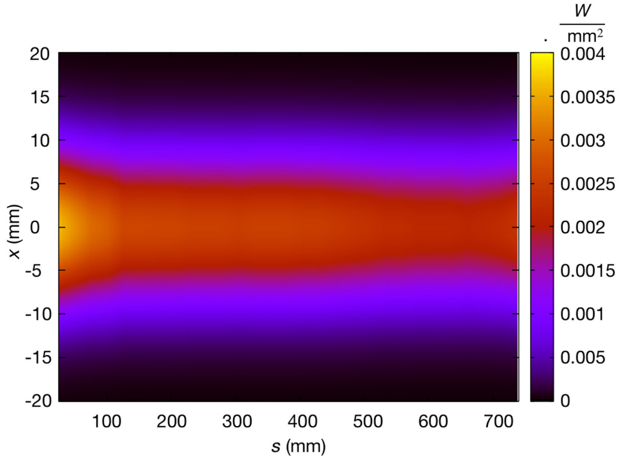

FIG. 4. Two-dimensional power density $P_1(s, x)$ deposited on the Ti-coating as a function of horizontal position x and longitudinal position s. SN003, $I_0 = 500$ mA.

$$P_{\mathrm{loss},n} = -T_0 \frac{I_0^2}{M} k_{\mathrm{loss},n}, \tag{11}$$

from which the following two-dimensional density is defined as [28]

$$P_1(s_n, x) = \frac{P_{\mathrm{loss},n}}{2\Delta} G(x). \tag{12}$$

The function $G(x)$ for the horizontal profile differs from Eq. (4) of [10] by a normalization factor, and in [27] it is shown that $G(x)$ fits well our computation. $P_1(s_n, x)$ for chamber SN003 and $I_0 = 500$ mA is shown in Fig. 4. The two-dimensional power density given by Eq. (12) is used as a input distribution for thermal analysis with the ANSYS code [29]. The fact that $P_1(s_n, x)$ is confined horizontally within dimensions smaller than the parallel sides of the chamber profile (approx. 31 mm) validates our parallel plate model.

IV. EXPERIMENTAL SETUP AND MEASUREMENT PROCEDURES

In order to benchmark the developed theory of beam-induced heating, spare ceramic chambers named SN003 and SN001 are used. The following sections will provide detailed information on the Ti-coating process and measurements of the resistivity of the ceramic chamber.

A. Ti-coating process and measurements

To solve the problem of Ti-coating quality, a new tool has been designed, built, and commissioned at NSLS-II (Fig. 5). The ceramic beampipe undergoes a physical vapor deposition (PVD) coating process using magnetron sputtering to apply a titanium layer. A vertical setup of titanium cathode wires is used within the ceramic chamber, where a plasma discharge is generated. This discharge is facilitated by a central anode rod, while an external solenoid applies a magnetic field to the ceramic chamber. This configuration facilitates the deposition of the titanium coating onto the ceramic surface.

FIG. 5. Ti-coating setup.

Witness coupons are installed just outside the end of the ceramic and a white light interferometer is used to measure the thickness step height. The longitudinal uniformity is checked with noncontact eddy-current measurements [30]. This measurement technique enables the assessment of coating thickness across the entire surface of the ceramic chamber.

After the coating process is completed, an annealing step is performed at a temperature of 400°C. This annealing step serves multiple purposes. First, it stabilizes the titanium film by allowing it to undergo an aging process, thereby reducing the occurrence of Eddy currents. Additionally, annealing helps to alleviate any stresses in the film that may have resulted from the deposition process. By dissolving surface oxides and nitrides into the bulk, annealing increases the resistivity of the coating. Furthermore, this annealing step acts as a final precautionary measure to prevent any blistering or flaking of the film due to thermal effects prior to installation.

B. Resistivity

Using the four-point probe resistance of the witness coupons and applying the appropriate correction factor for the four-point measurement [31], we derived the resistivity by using the coupon thickness measured by a white light interferometer. The measured average resistivity from a sample of high-quality-coated coupons is 3.85×10^{-6} Ωm. This value is considerably higher than some of the published values for deposited titanium thin films using e-beam evaporation and magnetron sputtering. However, it has been demonstrated that various factors can lead to variations in the resistivity of deposited thin films. The grain structure of deposited films is influenced by the deposition rate, the presence of incorporated impurities, arrival energy, and surface mobility due to sputtering power and target-to-substrate distance [32].

Furthermore, we found that annealing the film increased the measured resistivity of our deposited films by approximately 1.5 to 2 times. Due to the relatively low sputtering power and high pressure during the coating process, as well as the annealing procedure, the higher measured resistivity is not unexpected and is similar to that of SOLEIL [11].

A noncontact eddy-current probe was developed [30] to measure the relative coating thickness along the length of the ceramic chamber on both the top and bottom surfaces, ensuring the desired longitudinal uniformity is achieved. The film's uniformity is crucial to ensure consistent performance and reduce the likelihood of localized heating or impedance variations along the chamber. Calibration of the probe to directly measure thickness proved unsuccessful due to the significant difference in the resistivity of the deposited Ti films compared to that of purchased titanium sheets.

Because it is difficult to insert and calibrate the four-point probe inside the chamber, we opted for a two-point probe measurement. The flange-to-flange resistance of chambers SN001 and SN003, as measured by the two-point method, is 5.6 Ω and 4.2 Ω, respectively. In this study, we have assumed a uniform transverse coating thickness, resulting in average thicknesses of 3.2 and 4.3 μm for chambers SN001 and SN003, respectively. We normalized the relative coating thickness with 3.2 and 4.3 μm for chambers SN001 and SN003 to construct the longitudinal thickness profile, as illustrated in Fig. 6.

Nevertheless, we estimated the impact of a nonuniform transverse thickness on the accuracy of simulation results using a simple but realistic model. Let us assume the titanium-coating thickness is constant on the central flat part of the chamber cross section (see Fig. 1) and linearly decreases from a central thickness of τ_1 to $\alpha\tau_1$ at the left and right sides of the chamber. In a worst case of zero thickness at the sides ($\alpha = 0$), the τ_1 is 40% higher than the average $\langle\tau_1\rangle$. In practice, the thickness at the sides can be 20%–50% of the top/bottom thickness, depending on the coating process, and the uncertainty of the coating thickness used for the temperature simulations is within the range of 18%–30%.

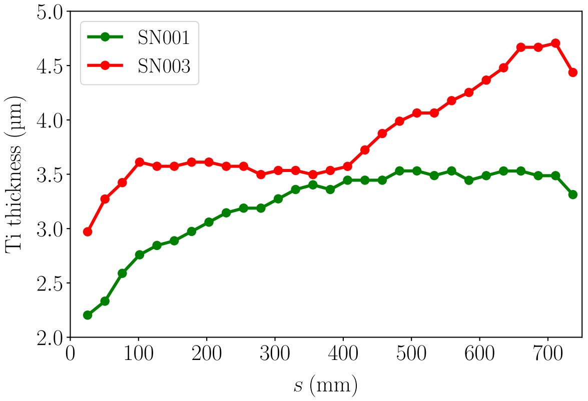

FIG. 6. Ti film thickness profile along the chambers SN001 and SN003.

V. THERMAL ANALYSIS

Thermal analysis using ANSYS [29] is a powerful tool for predicting the operating temperature of a ceramic chamber based on the analytically calculated heat load. Initial findings indicate that the results are highly sensitive to the film coefficient used for free convection calculations. We typically assume a value of film coefficient between 5 and 15 $\mathrm{W/m^2}$ °C but for this study, we need a more precise value to better predict steady-state temperature.

A. Measurements of film coefficient

The experimental setup consists of a $9.5\ \mathrm{mm} \times 94\ \mathrm{mm} \times 152\ \mathrm{mm}$ aluminum plate as shown in Fig. 7, serving as the main component [33]. Two 15 W heaters are mounted on the bottom surface of the plate, while the bottom and side edges are insulated with Nomex material, ensuring that only the top surface is exposed. To monitor the temperature, an RTD sensor is instrumented on the top surface of the plate. The setup is located in the NSLS-II

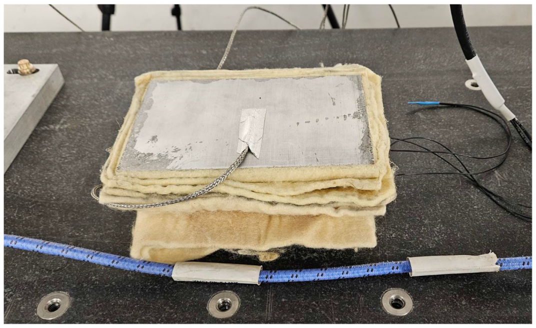

FIG. 7. Experimental setup to measure film coefficient.

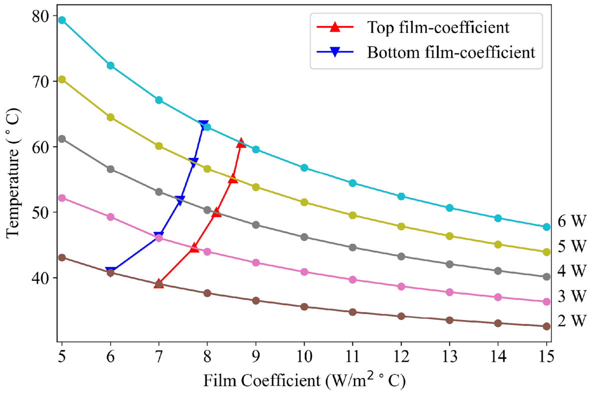

FIG. 8. Predicted temperatures as a function of the film coefficient for a given input power serves as the boundary condition. The points of intersection between the curves represent instances where the experimental top and bottom film coefficients align with the FEA model.

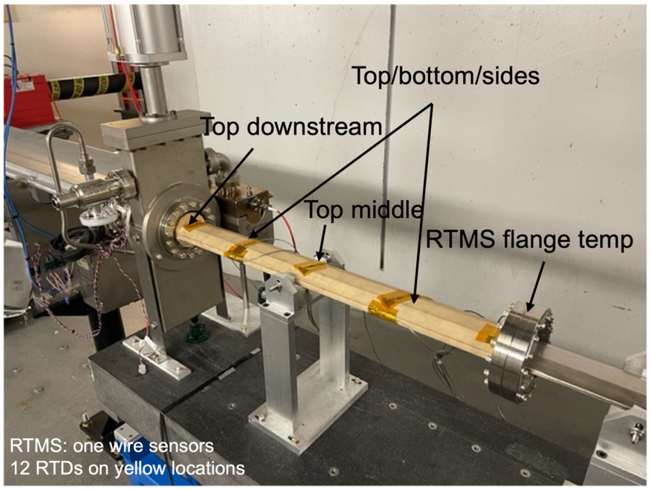

FIG. 9. Chamber setup with 12 RTDs placed in C01 at NSLS-II.

accelerator tunnel, close to the ceramic chamber, enabling controlled thermal interactions. To regulate the heat output, a remote-controlled power supply is employed, allowing for power adjustments ranging from 2 to 6 W. Throughout the experiment, temperature measurements are logged.

Figure 8 shows a set of predicted temperatures for different film coefficients with the finite element analysis (FEA) model of the plate. For each curve, a given power was the input boundary condition, and the convective film coefficient was varied from 5 to 15 $\mathrm{W/m^2\,°C}$. The resulting peak temperature was then plotted.

During the experiment, the power into the aluminum plate was regulated to match these curves, from 2 to 6 W. The plate was allowed to reach an equilibrium temperature, and these temperatures were also plotted on the same graph.

The experiment was repeated with the exposed surface of the aluminum plate facing downward to measure the bottom film coefficient. The points where these curves intersect with the curves of the plotted FEA results are where the experimental film coefficients agree with those used in the FEA.

For the top film coefficients, we see that the film coefficient value varies from 7 to 8.7 $\mathrm{W/m^2\,°C}$. For the bottom, we see that it varies from 6 to 7.9 $\mathrm{W/m^2\,°C}$. These empirically derived values of the convective film coefficient were used in the FEA of the ceramic chamber to more accurately predict temperature distributions for a given set of power densities.

B. Beam-based measurements

The processed chamber SN003 was installed in the test straight section C01 at NSLS-II, as shown in Fig. 9. This chamber was equipped with 12 resistance temperature detectors (RTDs) that were strategically positioned to monitor temperature variations within the chamber. We conducted a series of measurements at NSLS-II using an operational fill pattern of 1200 bunches with a total beam current of 500 mA. The beam current and temperatures measured by 12 sensors were archived and postprocessed. These measurements were done systematically over an extended period of time to ensure that the temperature reached equilibrium. To validate the results and ensure consistency, the same experiment was repeated for chamber SN001.

To confirm that the beam-induced power is dissipated in the titanium coating, as discussed in Sec. III C, the setup, as shown in Fig. 10, used the Electro-Metrics EM-6853 Ultra-Wideband Passive Omni-Directional Antenna to measure beam-induced power penetrating the ceramic chamber. This antenna, covering a wide frequency range from below 300 MHz to over 40 GHz, was positioned at both the upstream and downstream ends of the chamber.

Figure 11 shows the signals measured at the upstream ends of the ceramic chamber for a beam current of 400 mA in 1200 bunches. The measured power penetrating through the metal coating and ceramics was about 40 mW, and this value is negligible compared to the power dissipated in the coating layer.

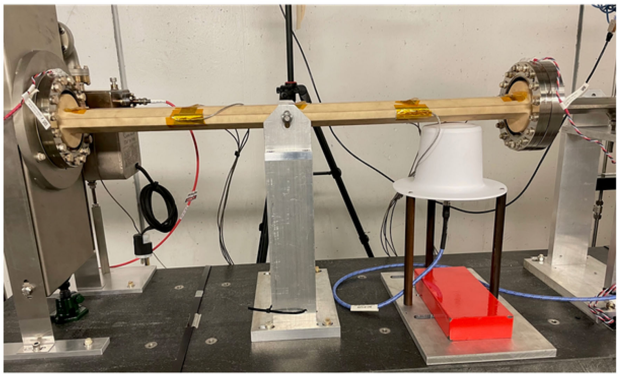

FIG. 10. Setup to measure the beam-induced power penetrating through ceramic chambers using an antenna C01 at NSLS-II.

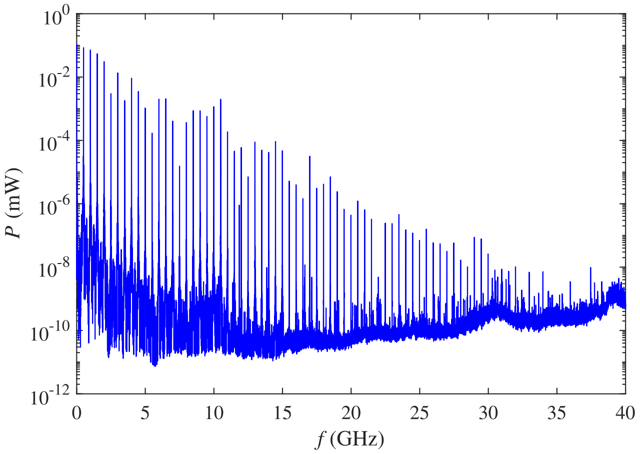

FIG. 11. Antenna signal at the upstream end of chamber for a beam current of 400 mA.

C. Comparison of measurements and simulations

The ANSYS simulation takes into account the measured Ti longitudinal thickness profile and the resistivity, which varies with temperature, to calculate the power density. The resistivity of the ceramic chambers, as discussed in Sec. IV B, has been measured at room temperature. To improve the accuracy of the analysis taking advantage of the knowledge of the equilibrium temperature measurements, the power density calculations have been performed assuming the following linear dependence of Ti resistivity on temperature:

$$\rho(T) = \rho_0[1 + \kappa(T - T_0)], \tag{13}$$

where $\rho_0 = 3.85 \times 10^{-6}$ Ωm is the measured resistivity at room temperature $T_0 = 20$°C and $\kappa = 3.6 \times 10^{-3}$/°C [34], and T is taken to be the average over s of the ceramics temperature measurements. The effect of including the resistivity variation with temperature improves the temperature analysis by approximately 20%. Figure 12 shows the computed power lost by the beam as a function of average beam current for chambers SN001 and SN003.

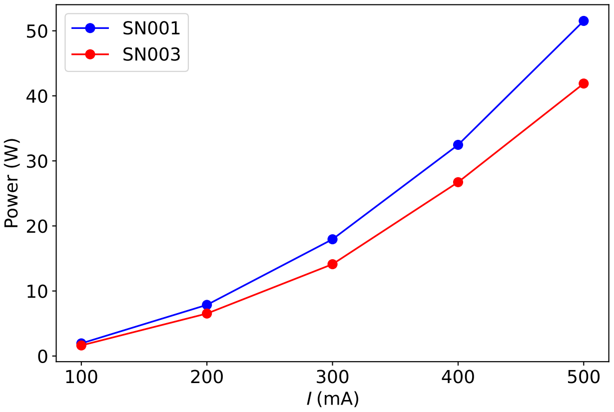

FIG. 12. Power lost by the beam as a function of average beam current for chambers SN001 and SN003.

For that given power density, convergence studies were conducted to integrate the measured film coefficient into the FEA model of the ceramic chamber to achieve optimal results. For the ceramic chamber ANSYS simulation, a variable heat source (Q_{in}) related to beam current that is power density, was applied to the chamber's inner surface. Additionally, we accounted for various heat dissipation mechanisms—conductive, convective, and radiative (Q_{out}) to ensure a comprehensive evaluation. This approach ensures our simulation accurately reflects the thermal behavior of the system.

This process involves a multistep simulation approach. First, we use an assumed film coefficient value base\d on prior experience and run ANSYS to determine the maximum temperature. Next, we project this temperature value onto the film coefficient curves shown in Fig. 8. The projected temperature values are used to determine a more precise film coefficient which is then used to perform a second iteration of ANSYS. This process is repeated until convergence is achieved.

Figure 13(a) presents a time-dependent temperature measurement of the SN003 chamber with a beam current of 500 mA. The graph illustrates that the temperature reaches equilibrium over time. In Fig. 13(b), a comparison between measured and simulated temperatures at various RTD locations on both the top and bottom of the chamber is presented. A snapshot of the ANSYS thermal analysis for this chamber is displayed in Fig. 13(c). Furthermore, Figs. 13(d) and 13(e) showcase the comparison of temperature measurements and simulations as functions of beam current ($I = 100$–500 mA) for the SN003 chamber at positions $s = 203.2$ mm (top sensor) and $s = 558.8$ mm (bottom sensor), respectively.

Similarly, Fig. 14(a) illustrates the temperature rise monitoring and the comparison between simulations and measurements at various RTD locations for chamber SN001, as shown in Fig. 14(b). Additionally, Figs. 14(c) and 14(d) present the comparison of temperature measurements and simulations as functions of beam current ($I = 100$–500 mA) for the SN001 chamber at positions $s = 203.2$ mm (top sensor) and $s = 558.8$ mm (bottom sensor), respectively.

The observed trends demonstrate a fair agreement of measurements and simulations within the range of maximum relative variation of 2%–8% at different beam currents. These results look promising for such a complex and multiparameter problem, considering that the discrepancies may arise from various factors, including experimental errors in thickness measurements, resistivity, film coefficient, and RTD calibration.

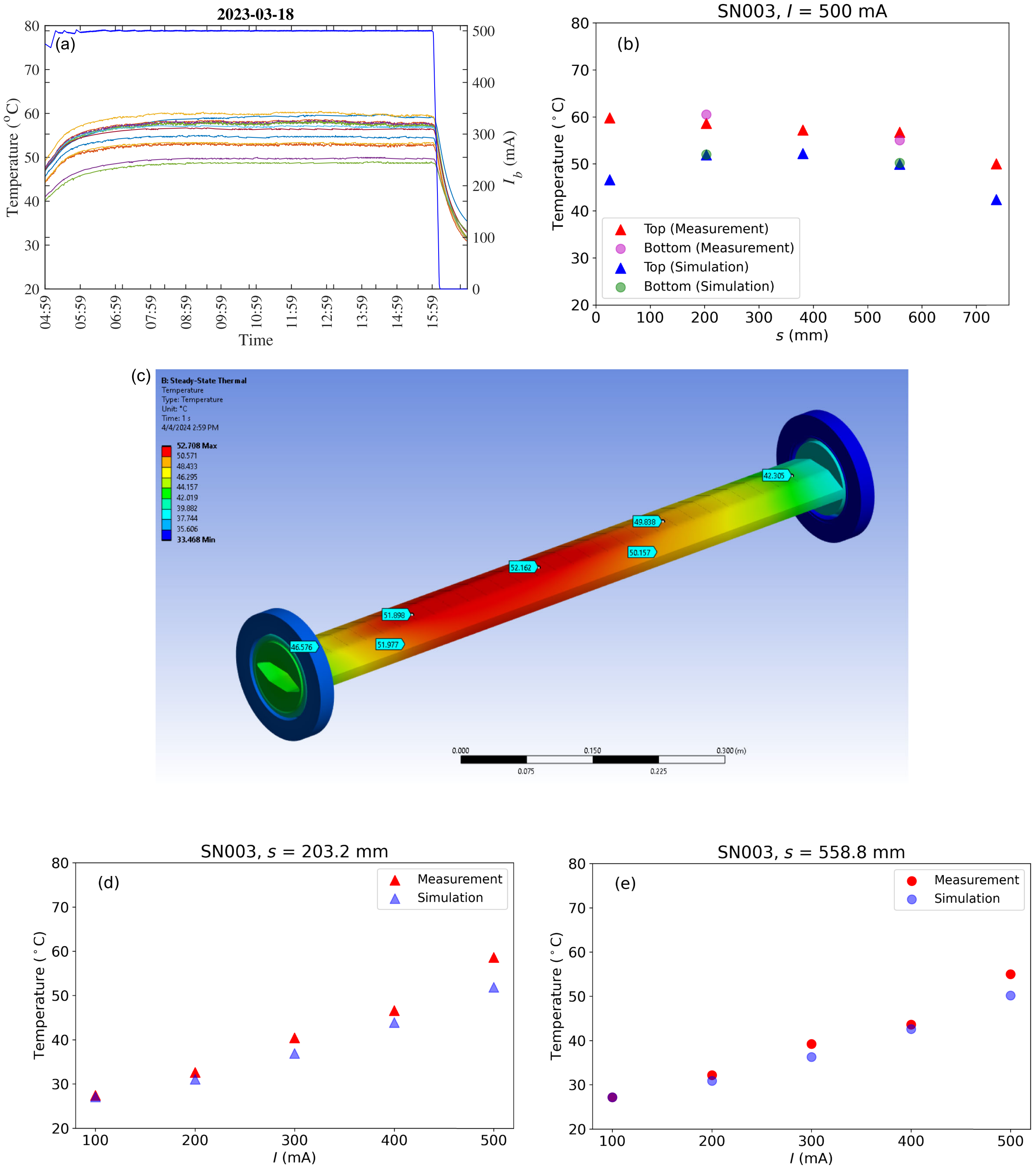

FIG. 13. Temperature rise monitoring over time for $I = 500$ mA at NSLS-II (a), along with a comparison between the measured and simulated temperatures at various RTD locations within chambers SN003 (b). A snapshot of the ANSYS thermal analysis for the SN003 chamber at $I = 500$ mA (c) is included. Additionally, a comparison of temperature measurements and simulations as a function of beam current for the SN003 chamber at two specific positions: (d) $s = 203.2$ (top sensor) and (e) $s = 558.8$ mm (bottom sensor).

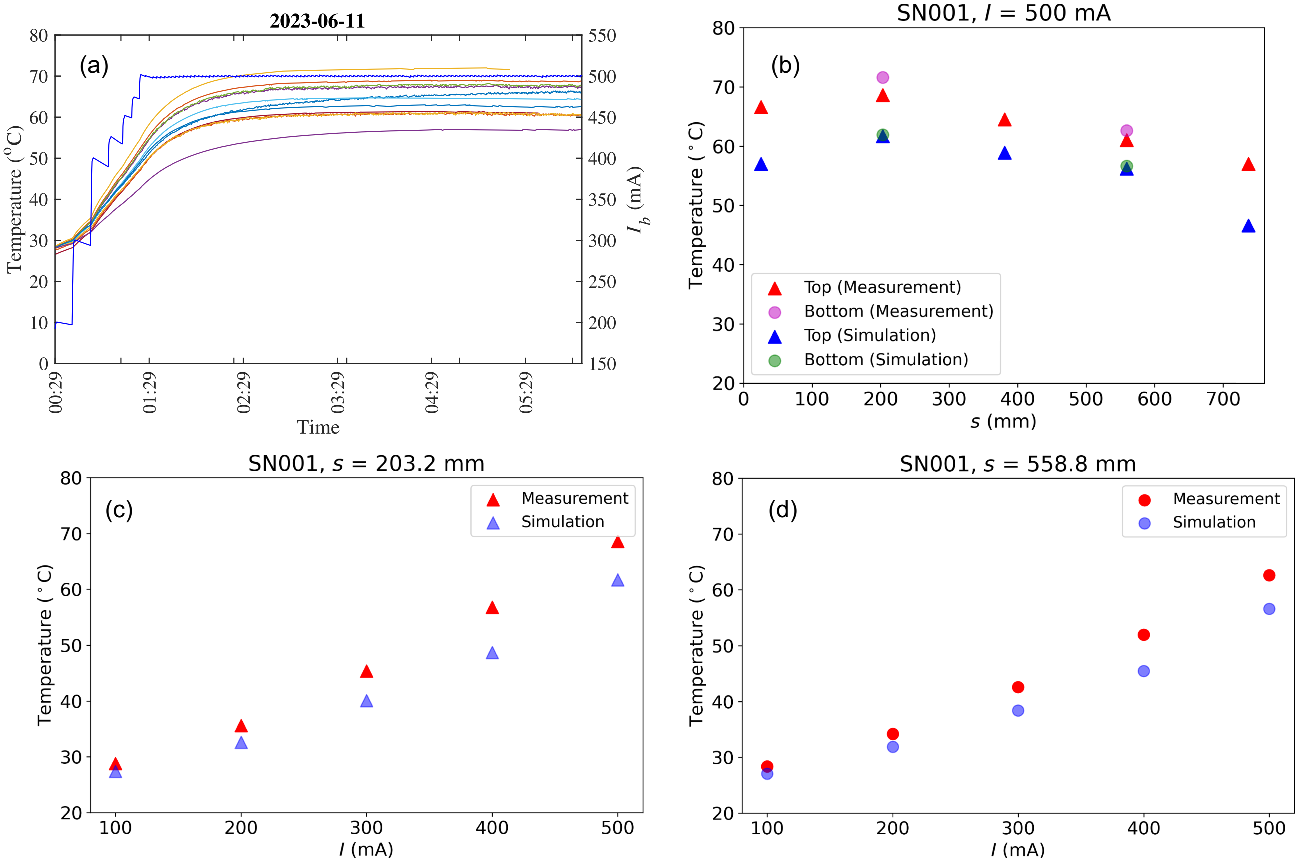

FIG. 14. Temperature rise monitoring over time for $I = 500$ mA at NSLS-II (a), along with a comparison between the measured and simulated temperatures at various RTD locations within chambers SN001 (b). A comparison of temperature measurements and simulations as a function of beam current for the SN001 chamber at two specific positions: (c) $s = 203.2$ mm (top sensor) and (d) $s = 558.8$ mm (bottom sensor).

VI. CONCLUSION

We summarized our studies of the impedance and beam-induced heating issues of titanium-coated ceramic vacuum chambers in the NSLS-II storage ring. Through rigorous analytical calculations and comparisons with numerical simulations, we have characterized the impedance of the two-layer electromagnetic system and demonstrated that the majority of power dissipation occurs on the titanium coating within the desired thickness range. Additionally, we showed that the longitudinally averaged two-dimensional power density is horizontally distributed according to a form given in [10]. This distribution, discussed in Sec. III C and illustrated in Fig. 4, facilitates the development of a simplified model for ANSYS simulations and subsequent thermal analysis. We also considered the measured thickness along the chamber and significant deviations of the measured titanium resistivity from reference book values [11]. Moreover, our findings emphasize the importance of considering the longitudinal variation of the Ti-coating thickness, the variation of resistivity with temperature, and a multistep simulation approach. These factors play a crucial role in accurate calculations of power density and thermal analysis. Furthermore, we have presented the variation of the film coefficient with temperature for a given power, highlighting another important factor to consider in the FEA of the chamber.

Our measurements and simulations exhibit relative variations of 2%–8% at different beam currents. The RTD calibration accuracy of 1–2°C contributes about 3%. It is important to note that these differences are well within expectations, given the potential influence of experimental variables, such as thickness measurements, resistivity, and film coefficients. We hope this study contributes to a better understanding of beam-induced heating and will be helpful for the reliable design of ceramic vacuum chambers for accelerator facilities.

ACKNOWLEDGMENTS

The authors would like to acknowledge with much appreciation Alexei Blednykh, Marcelo Juni Ferreira, and Timur Shaftan for their help. We would also like to acknowledge Alexis Gamelin and Patrick Alexandre from SOLEIL who responded to our queries regarding the techniques used there. This work has been supported by DOE under Contract No. DE-SC0012704.

[1] E. Huttel, Materials for accelerator vacuum systems, CERN European Organization for Nuclear Research, Report No. OPEN-2000-283, 1999, 10.5170/CERN-1999-005.237.

[2] S. S. Kurennoy, Using a ceramic chamber in kicker magnets, in *Proceedings of the International Conference on Particle Accelerators, Washington, DC* (IEEE, New York, 1993), pp. 3420–3422.

[3] A. W. Chao, M. Tigner, H. Weise, and F. Zimmermann, *Handbook of Accelerator Physics and Engineering* (World Scientific, Singapore, 2013).

[4] U. Iriso, T. Günzel, E. Koukovini-Platia, H. Bartosik, and G. Rumolo, Beam based impedance characterization of the ALBA pinger magnet, in *Proceedings of the 6th International Particle Accelerator Conference, IPAC-2015, Newport News, VA* (JACoW, Geneva, Switzerland, 2015), Vol. 15.

[5] R. Auchettl, R. Dowd, and Y. Tan, Beam dynamics, injection and impedance studies for the proposed single pulsed nonlinear injection kicker at the Australian Synchrotron, in *Proceedings of the 10th International Particle Accelerator Conference, IPAC-2019, Melbourne, Australia* (JACoW, Geneva, Switzerland, 2019).

[6] N. Mounet, N. Biancacci, and D. Amorim, ImpedanceWake2D, https://twiki.cern.ch/twiki/bin/view/ABPComputing/ImpedanceWake2D (2019).

[7] T. Atkinson, M. Dirsat, O. Dressler, P. Kuske, and H. Rast, Development of a non-linear kicker system to facilitate a new injection scheme for the BESSY II storage ring, *Proceedings of the 2nd International Particle Accelerator Conference, IPAC-2011, San Sebastian, Spain* (JACoW Publishing, Geneva, Switzerland, 2011), p. 3394, https://jacow.org/IPAC2011/papers/THPO024.pdf.

[8] S. White, Collective effects at ESRF, EIC Workshop 2021, https://meetings.triumf.ca/event/254/contributions/3129/attachments/2414/2764/EIC_CollectiveEffects.pdf (2021).

[9] D. Xu and W. Xu, Study on beam-induced heating in injection section of Hefei Light Source, J. Phys. Conf. Ser. **1350**, 012018 (2019).

[10] R. Nagaoka, J. Denard, and M. Level, Recent studies of geometric and resistive wall impedance at SOLEIL, in *Proceedings of the 10th European Particle Accelerator Conference, Edinburgh, Scotland, 2006* (EPS-AG, Edinburgh, Scotland, 2006).

[11] A. Gamelin, P. Alexandre, R. B. El Fekih, J. D. S. Castro, M. El Ajjouri, A. Letresor, L. Nadolski, R. Ollier, S. Thoraud, M. Sacko *et al.*, Investigation of rf heating for the multipole injection kicker installed at SOLEIL, J. Phys. Conf. Ser. **2420**, 012057 (2023).

[12] J. Kallestrup, P. Alexandre, Å. Andersson, R. Ben El Fekih, J. Breunlin, D. Olsson, P. Tavares, P. Alexandre, and R. B. Fekih, Studying the dynamic influence on the stored beam from a coating in a multipole injection kicker, in *Proceedings of the 10th International Particle Accelerator Conference, IPAC-2019, Melbourne, Australia* (JACoW, Geneva, Switzerland, 2019), pp. 19–24.

[13] A. Blednykh, B. Bacha, G. Bassi, G. Ganetis, C. Hetzel, H.-C. Hseuh, T. Shaftan, V. Smaluk, and G. Wang, Beam-induced heating of the kicker ceramics chambers at NSLS-II, in *2016 North American Particle Accelerator Conference, NAPAC-2016, Chicago, IL* (JACoW, Geneva, Switzerland, 2016).

[14] P. Alexandre, R. B. El Fekih, A. Letrésor, S. Thoraud, J. da Silva Castro, F. Bouvet, J. Breunlin, Å. Andersson, and P. F. Tavares, Transparent top-up injection into a fourth-generation storage ring, Nucl. Instrum. Methods Phys. Res., Sect. A **986**, 164739 (2021).

[15] D. Einfeld, The ceramic chambers of ESRF-EBS, https://indico.cern.ch/event/819665/contributions/3494644/attachments/1877421/3093169/ESRF-Ceramic-Chambers.pdf (2019).

[16] C. Laasch, NSLS-II achieves design beam current of 500 milliamperes, https://www.bnl.gov/nsls2/newsletter/news.php?a=217026 (2020).

[17] G. Bassi, A. Khan, B. Kosciuk, V. Smaluk, R. Todd, C. Hetzel, M. Seegitz, and A. Blednykh, Analysis of beam-induced heating of the NSLS-II ceramic vacuum chambers, in *Proceedings of the 5th North American Particle Accelerator Conference, NAPAC 2022, Albuquerque, NM* (JACoW, Geneva, Switzerland, 2022).

[18] A. Blednykh, G. Bassi, Y. Hidaka, V. Smaluk, and G. Stupakov, Low-frequency quadrupole impedance of undulators and wigglers, Phys. Rev. Accel. Beams **19**, 104401 (2016).

[19] G. Bassi, Analytical formulae for the longitudinal impedance of two parallel layers with arbitrary complex permittivity and permeability, in *Proceedings of the 14th International Particle Accelerator Conference, IPAC 2023* (JACoW, Geneva, Switzerland, 2023), pp. 3381–3384.

[20] G. Bassi, Impedance analysis and power dissipation of a metallic-coated ceramic chamber in planar approximation (to be published).

[21] We remind the reader that Eq. (1) is valid for a two parallel plate model.

[22] N. Mounet and E. Métral, Electromagnetic fields and beam coupling impedances in a multilayer flat chamber, CERN, Technical Report, 2010.

[23] N. Mounet, The LHC transverse coupled-bunch instability, EPFL, Technical Report No. CERN-THESIS-2012-055, 2012.

[24] J. D. Jackson, *Classical Electrodynamics* (John Wiley & Sons, New York, 2021).

[25] This approximation simplifies the analysis by neglecting energy dissipation due wakefields generated by nearby geometries such as tapers.

[26] L. Teofili, M. Migliorati, D. Carbajo, F. Giordano, I. Lamas, and G. Mazzacano, A multi-physics approach to simulate the rf-heating 3d power map induced by the proton beam in a beam intercepting device, J. Phys. Conf. Ser. **1067**, 062012 (2018).

[27] G. Bassi, Power dissipation on the metallic coating of a ceramic chamber in planar approximation, Photon Sciences, Brookhaven National Laboratory, Technical Note No. NSLSII-ASD-TN-415, BNL-225654-2024-TECH, 2024.

[28] Using Eqs. (10) and (11), the three-dimensional integral $\int\int\int ds\,dx\,dy\,P_3(s,x,y)$ over the metal coating reads $-T_0\frac{I_0^2}{M}\sum_{n=1}^{N}\frac{k_{\mathrm{loss},n}}{2\Delta\tau_1(s_n)}\int_{s_n}^{s_n+\Delta}ds\int_0^{\tau_1(s_n)}dy\int G(x)dx = -T_0\frac{I_0^2}{M}\sum_{n=1}^{N}\frac{k_{\mathrm{loss},n}}{2} = \frac{P_{\mathrm{loss},T}}{2}$, where in the last equality we used

Eq. (7). Thus half of the total power lost by the beam is dissipated on one of the two metal coatings.

[29] P. Kohnke, *Finite Element Systems: A Handbook* (Springer, Berlin, Germany, 1982), pp. 19–25.

[30] J. Escallier, Non-contact based measurement of thin film coatings using eddy current measurements, Photon Sciences, Brookhaven National Laboratory, Technical Note No. NSLSII-ASD-TN-404, BNL-225309-2024-TECH, 2024.

[31] F. Smits, Measurement of sheet resistivities with the four-point probe, Bell Syst. Tech. J. **37**, 711 (1958).

[32] N. Muslim, Y. Soon, C. Lim, and N. Voo, Influence of sputtering power on properties of titanium thin films deposited by rf magnetron sputtering, ARPN J. Eng. Appl. Sci. **10**, 7184 (2015), https://api.semanticscholar.org/CorpusID:44049292.

[33] The measurement of the film coefficient is independent of the material used, being determined by the heat transfer fluid's characteristics, fluid velocity, and flow regime. In our experiment, air was used as the fluid under static or near-static conditions with buoyancy-driven flow. The results would have remained consistent even if a ceramic plate was used, with the only difference being the time required to reach a steady state due to the varying thermal conductivities between the materials.

[34] M. Angadi, Some transport properties of transition metal films, J. Mater. Sci. **20**, 761 (1985).